Journal of The Electrochemical Society

The Electrochemical Society
Advancing solid state & electrochemical science & technology

Influence of A-Site Modifications on the Properties of $La_{0.21}Sr_{0.74-x}Ca_xTi_{0.95}Fe_{0.05}O_{3-\delta}$ Based Fuel Electrode for Solid Oxide Cell

To cite this article: S. Paydar *et al* 2023 *J. Electrochem. Soc.* **170** 054502

Journal of The Electrochemical Society, 2023 **170** 054502

Influence of A-Site Modifications on the Properties of $La_{0.21}Sr_{0.74-x}Ca_xTi_{0.95}Fe_{0.05}O_{3-\delta}$ Based Fuel Electrode for Solid Oxide Cell

S. Paydar,[1] K. Kooser,[2] P. Möller,[1] O. Volobujeva,[3] S. Granroth,[4] E. Lust,[1] and G. Nurk[1,z]

[1]*Institute of Chemistry, University of Tartu, Tartu 50411, Estonia*
[2]*Institute of Physics, University of Tartu, 50411 Tartu, Estonia*
[3]*Department of Materials Science, Tallinn University of Technology, 19086 Tallinn, Estonia*
[4]*Department of Physics and Astronomy, University of Turku, 20014 Turku, Finland*

To make solid oxide fuel cell (SOFC) systems commercially attractive it's essential to reduce manufacturing cost and improve the stability of membrane electrode assembly (MEA). In this research, the influence of A-site modification on electrical and electrochemical performance of 5% A-site deficient $La_{0.21}Sr_{0.74-x}Ca_xTi_{0.95}Fe_{0.05}O_{3-\delta}$ (x = 0.26 − 0.69) (LSCTF5-x) hydrogen electrode has been studied. Results indicate that the magnitude of A-site deficiency and Ca concentration in A-site influence the conductivity, catalytic activity and stability of the electrodes considerably. The highest stability was observed in the case of $La_{0.21}Sr_{0.26}Ca_{0.48}Ti_{0.95}Fe_{0.05}O_{3-\delta}$ anode composition. The maximal total electrical conductivity of porous electrode layer made of LSCFT5-x was 3.5 S cm^{-1} at 850 °C characteristic of the $La_{0.211}Sr_{0.26}Ca_{0.48}Ti_{0.95}Fe_{0.05}O_{3-\delta}$ material in 97% H_2 + 3% H_2O atmosphere. The best electrochemical performance was observed in the case of $La_{0.21}Sr_{0.37}Ca_{0.37}Ti_{0.95}Fe_{0.05}O_{3-\delta}$, which showed polarization resistance value equal to 0.44 Ω cm^2 after 100 h of stabilization at 800 °C in humidified (1.7% H_2O) H_2 atmosphere. During the stability test the fuel cell with optimal anode composition 50 wt% $La_{0.21}Sr_{0.26}Ca_{0.48}Ti_{0.95}Fe_{0.05}O_{3-\delta}$ + 50 wt% $Ce_{0.9}Gd_{0.1}O_{2-\delta}$ showed power density of 437 mW cm^{-2} at 850 °C in 98.3% H_2 + 1.7% H_2O atmosphere.

[DOI: 10.1149/1945-7111/acd084]

Manuscript submitted December 30, 2022; revised manuscript received March 22, 2023. Published May 9, 2023.

Supplementary material for this article is available online

Highly efficient and low-cost conversion between chemical and electrical energy is one of the key challenges for future society using renewable energy sources. Solid oxide fuel cell (SOFC) as a fuel flexible and highly efficient energy conversion device can be considered as one of the key components of the future energy concept.[1–3] Ni-cermet as typical SOFC hydrogen electrode material displays outstanding catalytic performance in hydrogen, but there are several issues related to this electrode, as poor sulfur tolerance, moderate redox stability and Ni-coarsening.[4–7] In addition, quick carbon deposition at operating temperatures, when carbon containing fuels are used, is another limitation of Ni-cermet electrodes application.[7,8] Therefore, there is a growing interest to explore new materials and replace the Ni-cermet fuel electrodes in order to eliminate these drawbacks.

Perovskite type complex oxides (ABO_3) with mixed ionic-electronic conductivity (MIEC) are attractive candidates for replacement of Ni-cermet SOFC anodes.[9,10] These electrodes have several advantages: (i) electrochemical reaction can take place on two-phase boundaries (electrode-gas interface) instead of triple-phase boundaries in Ni-cermets;[11] (ii) good redox stability; (iii) high sulfur and carbon tolerance which results from good availability of oxygen from MIEC material to reaction sites.[12] Additionally, the great advantage of MIEC materials compared to Ni-cermets is the minor coarsening effects observed at ceramic electrodes.[13,14]

Perovskites type complex oxides (ABO_3) such as lanthanum doped strontium titanates, $La_xSr_{1-x}TiO_{3-\delta}$ (LST) have attracted particular attention as a promising candidate for SOFC anode application over the past years. In perovskite oxides (ABO_3), the electronic conduction is believed to occur by the small polaron hopping mechanism, the electrons hoping between multivalent B-site ions and oxygen ions along –B–O–B– bonds.[15] Several different compositions have been studied to optimize doping levels and stoichiometry of LST for improving catalytic activity, electrical conductivity and chemical stability.[16,17] However, limited catalytic activity and low conductivity are so far the most common throwbacks for MIEC electrodes and therefore activation of these materials is necessary. The redox exsolution method has been used to increase the catalytic activity of MIEC interfaces.[18,19] Different strategies, such as modification of cation stoichiometry and chemical composition as well as a controlled change of stoichiometry between A and B sites have been employed to drive exsolution.[20,21] One strategy to arouse exsolution and alleviate A-site cation segregation is using the non-stoichiometric perovskite with $A/B < 1$.[21,22] In these non-stoichiometric perovskite oxides with A-site deficiency the valence states of the B-site cations effectively increase, and thus, enhance the stability of the BO_6 octahedral structure. However, such a decrease of the concentration of the A-site centers increases thermodynamic instability of the perovskite and inducing B-site cation segregation to stabilize the oxide structure. It has been demonstrated, that increase of A-site deficiency in $SrTiO_3$-based perovskite with donor doping on Sr or Ti site could remarkably increase oxygen vacancy concentration, which can contribute to enhance the ionic conductivity of electrodes.[22–26] Similarly, the A-site deficient $SrTiO_3$ materials exhibit much higher electronic conductivity at low oxygen partial pressures compared with non A-site deficient ones.[24,27] Moreover, A-site deficiency coupled with reducible transition metal catalyst has been used to enhance the electrocatalytic activity of oxide anode.[24,28–30] Furthermore, deficiency in the A-site also suppresses effectively Sr segregation and mobility. Lee et al. also reported that A-site deficient $(La_{0.8}Sr_{0.2})_{1-x}MnO_{3-d}$ $(x > 0)$ films show higher chemical stability against Sr segregation upon thermal annealing, whereas over-stoichiometry $(x < 0)$ facilitates segregation.[31] This strategy can be employed for optimization of physical and chemical properties of solid oxide fuel cell electrode materials.[32]

Moreover, the introduction of calcium (Ca) into A-site of LST decreases the unit cell volume and expedites the reduction of fuel. Calcium doping also improves the sinterability of LST structure.[13,23] Further B-site doping with transition metals (Fe, Ni) for LST can improve the conductivity as well as the catalytic activity of LST fuel electrode.[33,34]

---

[z] E-mail: gunnar.nurk@ut.ee

Table I. Stoichiometries and abbreviations of studied $La_{0.21}Sr_{0.74-x}Ca_xTi_{0.95}Fe_{0.05}O_{3-\delta}$ (LSCTF5-x) and $La_{0.2}Sr_{0.7-x}Ca_xTi_{0.95}Fe_{0.05}O_{3-\delta}$ (LSCTF10-x)[35] powders.

Stoichiometry of interest	Abbreviation
$La_{0.21}Sr_{0.48}Ca_{0.26}Ti_{0.95}Fe_{0.05}O_{3-\delta}$	LSCTF5–26
$La_{0.21}Sr_{0.37}Ca_{0.37}Ti_{0.95}Fe_{0.05}O_{3-\delta}$	LSCTF5–37
$La_{0.21}Sr_{0.26}Ca_{0.48}Ti_{0.95}Fe_{0.05}O_{3-\delta}$	LSCTF5–48
$La_{0.21}Sr_{0.16}Ca_{0.58}Ti_{0.95}Fe_{0.05}O_{3-\delta}$	LSCTF5–58
$La_{0.21}Sr_{0.05}Ca_{0.69}Ti_{0.95}Fe_{0.05}O_{3-\delta}$	LSCTF5–69
$La_{0.2}Sr_{0.45}Ca_{0.25}Ti_{0.95}Fe_{0.05}O_{3-\delta}$[35]	LSCTF10–25
$La_{0.2}Sr_{0.35}Ca_{0.35}Ti_{0.95}Fe_{0.05}O_{3-\delta}$[35]	LSCTF10–35
$La_{0.2}Sr_{0.25}Ca_{0.45}Ti_{0.95}Fe_{0.05}O_{3-\delta}$[35]	LSCTF10–45
$La_{0.2}Sr_{0.15}Ca_{0.55}Ti_{0.95}Fe_{0.05}O_{3-\delta}$[35]	LSCTF10–55
$La_{0.2}Sr_{0.05}Ca_{0.65}Ti_{0.95}Fe_{0.05}O_{3-\delta}$[35]	LSCTF10–65

In this study the influence of A-site modifications on the physical properties, electrical and electrochemical performance of 5% A-site deficient $La_{0.21}Sr_{0.74-x}Ca_xTi_{0.95}Fe_{0.05}O_{3-\delta}$ ($x = 0.26 - 0.69$) (LSCTF5-x) hydrogen electrode has been investigated. The properties of LSCTF5-x, described in this study have been compared to properties of $La_{0.2}Sr_{0.7-x}Ca_xTi_{0.95}Fe_{0.05}O_{3-\delta}$ (LSCTF10-x) with 10% A-site deficiency with exactly the same La/Sr/Ca ratios as well as the same techniques used for synthesis and testing of the electrodes.[35]

Experimental

Materials synthesis.—The raw powders for preparing of $La_{0.21}Sr_{0.74-x}Ca_xTi_{0.95}Fe_{0.05}O_{3-\delta}$ (LSCTF5-x with 5% A-site deficiency) ($x = 0.26 - 0.69$ and represent the amount of Ca in lattice) fuel electrodes were synthesized by using the glycine-nitrate combustion synthesis method from the high-purity starting chemicals of $La(NO_3)_3.6H_2O$ (99.9%, Alfa Aesar), $Sr(NO_3)_2$ (99.9%, Alfa Aesar), $Ca(NO_3)_2.4H_2O$ (99.9%, Alfa Aesar), $Fe(NO_3)_3.9H_2O$ (99.9%, Alfa Aesar) and $C_6H_{22}N_2O_8Ti$ 50% solution in water (Sigma- Aldrich) and glycine (99%, Sigma Aldrich) as reducing agent. The mole ratio of the nitrate to glycine was fixed at 1:0.7. Exact concentrations of the precursor solutions were determined using thermogravimetric analysis (STA 449 F3 Jupiter, Netzsch) for each metal cation raw solution. The powder received from glycine-nitrate combustion synthesis was calcinated at 1100 °C for 20 h to improve the crystallinity of perovskite structured LSCTF5-x. Following additives were used to make screen-printing paste from the raw-powder: α-terpineol (SAFC) as a solvent, Solsperse 3000 (Lubrizol) as a dispersant, polyethene glycol (Sigma Aldrich) as a binder and polyvinyl butyral (Sigma Aldrich) as a plasticizer. Table SI in supplementary displays sintering temperatures of all prepared layers. Table I shows the exact stoichiometry of 5% A-site deficient powders synthesised in this study (LSCTF5-x) and powders with 10% A-site deficiency (LSCTF10-x) synthesized, characterized and analyzed using the same protocol and equipment.[35] The proportions of La, Sr and Ca are same in both experimental sets only different the magnitude of A-site deficiency has been considered.

Electrical- and electrochemical measurements.—The electrical conductivity of porous LSCTF5-x electrodes was measured by the standard four-probe method. For preparing samples alumina plates with 250 μm thickness as substrate were used. Approximately 20–30 μm thick LSCTF5-x electrodes were screen printed onto the alumina substrates (1 cm^2 geometric surface area). Then the porous layers were sintered at 1250 °C for 5 h. Four Pt electrodes at precise distance were printed onto the porous MIEC electrode and thermally treated after that. The fuel cell tests and symmetrical cell experiments were carried out on the $(Sc_2O_3)_{0.10}(CeO_2)_{0.01}(ZrO_2)_{0.89}$ (ScCeSZ) (Kerafol) electrolyte membranes with 250 μm thickness. A $Gd_{0.1}Ce_{0.9}O_{2-\delta}$ (GDC) (ESL Europe, type 4343) barrier layer was screen printed onto both sides of the electrolyte to avoid reactions between MIEC oxide material and zirconia. Fuel electrode with approximately 20 μm thickness and 0.50 cm^2 active area was screen printed onto GDC barrier layer of both sides for symmetrical cell tests. GDC (Fuel Cell Materials) powder (to improve ionic conductivity) mixed with LSCTF5-x (1:1 wt% ratio) were used for preparing of the screen-printing paste for preparing of the symmetrical cell electrodes and the fuel cell anodes. For fuel cell measurements, $La_{0.6}Sr_{0.4}Co_{0.96}Ti_{0.04}O_{3-\delta}$ (LSCT) as a cathode was screen-printed symmetrically with an anode to the other side of the electrolyte membrane onto the GDC barrier layer. Complete description of cathode paste preparation has been presented in our earlier study.[36] In fuel cell setup platinum current collectors were screen printed onto both electrodes using commercial Pt-ink (Fuel Cell Materials). Solid oxide fuel cell tests were conducted only for two-unit cells, LSCTF5–35 and LSCTF5–45 with the most active anode composition. All measurements were carried out in Carbolite VST 1200 furnace in temperature range from 650 to 850 °C. To perform electrochemical and conductivity measurements Solartron 1287 A potentiostat/galvanostat and a Solartron 1260 frequency response analyzer were used. Impedance spectra with the AC voltage amplitude of 10 mV and the frequency range from 0.01 Hz to 100 KHz were recorded.

All conductivity- and electrochemical measurements were carried out at gas overflow conditions, to keep pre-defined gas composition everywhere on top of the studied electrode. Gas flows were controlled using EL-FLOW SELECT F–201CV mass flow controllers (Bronkhorst). Two different gas compositions were used during electrical conductivity studies and electrochemical measurements of symmetrical cells: $1\%H_2 + 3\%\ H_2O + 96\%$ Ar and $97\%\ H_2 + 3\%\ H_2O$, which correspond to $pO_2 = 4 \times 10^{-17}$ atm and $pO_2 = 4 \times 10^{-21}$ atm at 850 °C and $pO_2 = 4 \times 10^{-22}$ atm and $pO_2 = 4 \times 10^{-26}$ atm at 650 °C, respectively.

Impedance analysis of fuel cells were performed under specific fixed cell potentials (at OCV and −0.9 V). Cyclic voltammograms were recorded using a scan rate of 5 mV s^{-1}. In the fuel electrode compartment, humidified hydrogen was used, thoes the used fuel mixture was conducted through a gas washing bottle containing MilliQ+ water conditioned in water circulator at 15 °C (1.7% H_2O uptake). In the oxygen electrode compartment synthetic air (79% N_2, 21% O_2) was used during fuel cell measurements.

Physical characterization of the material.—To detect the crystal structure and purity of phase, Bruker-AXS D8 X-ray diffractometer with a Cu Kα radiation source (40 kV, 40 mA, a Goebel mirror, 2.5° Soller slits and LynxEye 1D detector) was used. The lattice parameters were calculated using Topas 6 software, the XRD maxima were fitted using Fundamental Parameters peak type and using known Au lattice parameters as a reference. The crystalline size of all pellets was calculated by Scherrer equation.

Cross-sections of cells and electrodes were characterized before and after the electrochemical experiments with a high-resolution scanning electron microscope (HR-SEM Zeiss Merlin) and time-of-flight secondary ion mass spectrometer (TOF-SIMS) (PHI TRIFT V nanoTOF instrument) to investigate the chemical and microstructural changes in electrode during sintering and during cell operation.

X-ray Photoelectron Spectroscopy measurements of all samples were carried out by Thermo Scientific Nexsa system at Turku University. This system enables monochromatized Al K-alpha radiation beam and uses hemispherical energy analyzer. Curve fitting analysis of all photoelectron spectra has been conducted with the SPANCF package.[37,38]

Results and Discussion

Physical characterization.—In Fig. 1 X-ray diffraction (XRD) patterns for all synthesized LSCFT5-x powders are presented. In the case of all samples characteristic reflections of perovskite structure

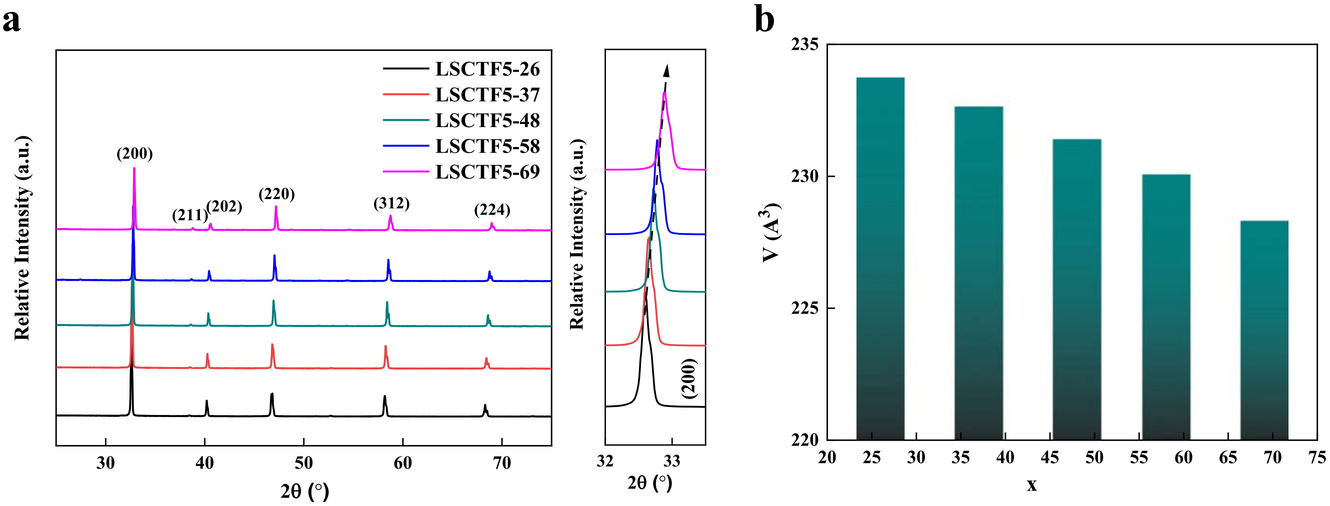

Figure 1. (a) XRD patterns of $(La_{0.2}Sr_{0.7\text{-}x}Ca_x)_{1.055}Ti_{0.95}Fe_{0.05}O_{3-\delta}$ (LSCTF5-x) (x = 0.26 – 0.69) powders at room temperature, (b) Relative changes in the unit cell volume of LSCTF5-x caused by changes of Ca content in the materials prepared (*x* corresponds to Ca mol% in the A-site).

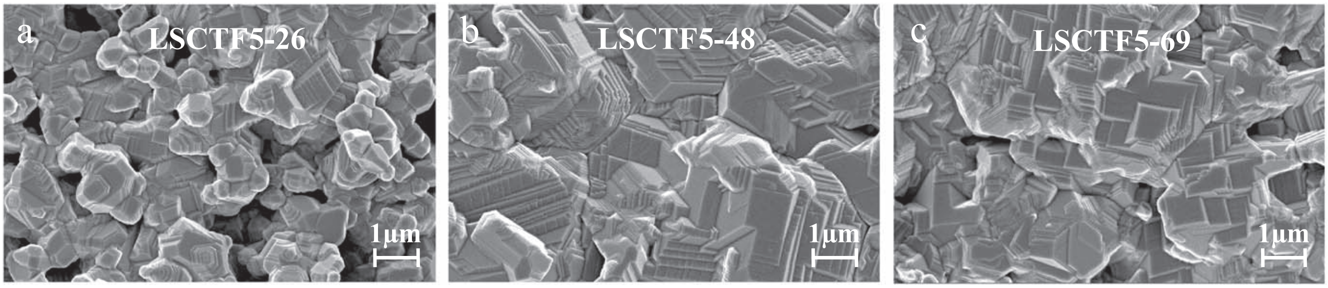

Figure 2. SEM images of porous (a) $La_{0.21}Sr_{0.48}Ca_{0.26}Ti_{0.95}Fe_{0.05}O_{3-\delta}$ (LSCTF5−26), (b) $La_{0.21}Sr_{0.26}Ca_{0.48}Ti_{0.95}Fe_{0.05}O_{3-\delta}$ (LSCTF5−48) and (c) $La_{0.21}Sr_{0.05}Ca_{0.69}Ti_{0.95}Fe_{0.05}O_{3-\delta}$ (LSCTF5−69) electrodes after 5 h sintering in air at 1250 °C.

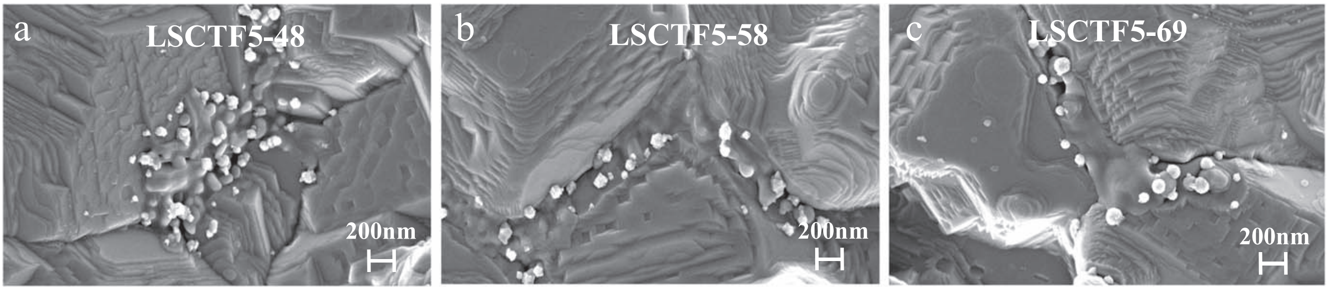

Figure 3. SEM images of (a) $La_{0.21}Sr_{0.26}Ca_{0.48}Ti_{0.95}Fe_{0.05}O_{3-\delta}$ (LSCTF5−48), (b) $La_{0.21}Sr_{0.16}Ca_{0.58}Ti_{0.95}Fe_{0.05}O_{3-\delta}$ (LSCTF5−58) and (c) $La_{0.21}Sr_{0.05}Ca_{0.69}Ti_{0.95}Fe_{0.05}O_{3-\delta}$ (LSCTF5−69) electrodes sintered in air and heat treated during 100 h at 1000 °C in 100% H_2 atmosphere.

could be detected. No secondary phase is observed for all diffraction patterns of LSCTF5-x samples. A closer inspection of the reflections shows that the characteristic peaks of LSCTF5-x gradually move toward higher reflection angles with the increasing of Ca concentration (Fig. 1a). The peak shift suggests that Ca^{2+} (1.14 Å) has effectively replaced by the larger Sr^{2+} (1.32 Å) ions. In addition, the unit cell volume of all LSCTF5-x samples was calculated and given in Fig. 1b. These results confirm that increasing for Ca concentration leads to the decrease of LSCTF5-x unit cell volume, similarly as in the case of LSCTF10-x.[35,39]

SEM micrographs of LSCTF5–26, LSCTF5–48 and LSCTF5–69 pellet surfaces after sintering at 1250 °C for 5 h in the air were recorded and are presented in Fig. 2. According to data in Fig. 2 all samples have highly crystalline structure. In addition, the grain size and sinterability of LSCTF5-x porous electrodes are almost comparable with LSCTF10-x material (with 10% A-site deficiency)[35] with same amount of Ca in lattice. Highest crystallinity, as well as grain size, can be seen for LSCTF5–48.

Electrode material surfaces were also studied by SEM analysis after treatment in H_2 environment at 1000 °C, due to investigate the degradation and stabilization processes appearing in the fuel electrodes with different amount of Ca in A-site and 5% A-site deficiency at high temperature in reducing atmosphere. Figure 3 shows the SEM micrographs of LSCTF5–48, LSCTF5–58 and LSCTF5–69 pellet surfaces after reduction in H_2 atmosphere during 100 h at 1000 °C. A number of small particles with diameters approximately 10–20 nm is noticeable on the surface of all electrodes, dominantly in the grain boundary region, but not only. SEM-EDX analysis data suggest that these are particles with high iron content (shown in Fig. S1). The EDX spectra also contains

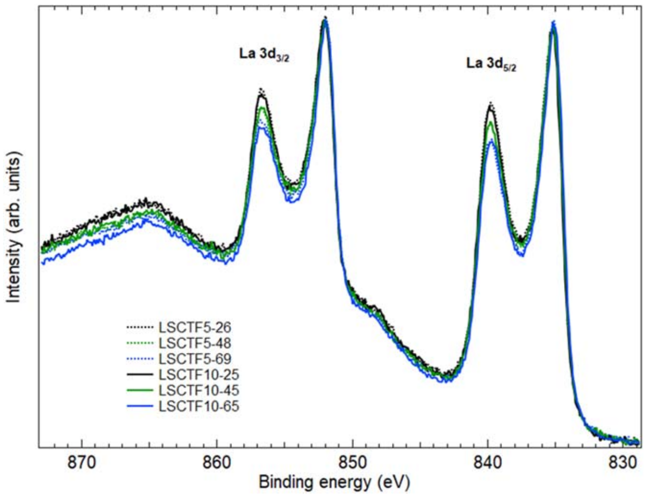

Figure 4. Photoelectron spectra of La 3d lines. The notation of studied samples is given in figure.

significant amount of background information and therefore precise detection of the chemical composition of these particles is not possible using only this method.

***Photoelectron spectra of synthesized LSCTF samples.*—**To estimate the chemical properties of the studied samples the X-ray Photoelectron Spectroscopy measurements were executed. This surface sensitive characterization technique was used to record the signal of La 3d, La 4d, Sr 3d, Ti 2p, Ca 2p, Fe 2p and O 1s photoelectron spectra of all LSCTF samples. The photon source was monochromatized Al K-alpha radiation (1486.6 eV). Also, the C 1s signal was used for the binding energy calibrations of photoelectron spectra.

The comparison of La 3d photoelectron spectra for LSCTF10–25, LSCTF5–26, LSCTF10–45, LSCTF5–48, LSCTF10–65 and LSCTF5–69 are depictured in Fig. 4. The main variations in spectra can be correlated to the changes of concentrations of Ca and Sr No remarkable dependence on the variation of the magnitude of A-site deficiency (from 5% to 10%) can be detected in these samples. The spin–orbit separation of La 3d$_{3/2}$ and La 3d$_{5/2}$ components is approximately 16.8 eV in all spectra measured. The multiple splitting value, ~4.6 eV, coincides to the corresponding result of La_2O_3 and is much bigger than multiplet splitting differences in $La(OH)_3$ or in $La_2(CO_3)_3$, 3.9 eV and 3.5 eV, respectively. However, the influence of reducing and oxidizing atmosphere to the LSCTF10–45 and LSCTF5–48 samples shows some differences in photoelectron spectra of La 3d lines. The given spectra in Figs. 5a, 5b clearly indicate to the broadening effect by more than 0.1 eV in oxidizing environment compared to the reducing environment which indicates slight change of chemical environment (surrounding ions) of La^{3+} cations. Similarly, to A-site elements, the loss or gain of electrons is detected also in the case of B-site elements of the studied samples. The Ti 2p photoelectron signal of LSCTF10–45, LSCTF5–48 samples, which were exposed in reducing (H_2) and in oxidizing (air) environment are presented in Figs. 5c, 5d. All these spectra contain clearly separated Ti 2p$_{3/2}$ (~459.5 eV), Ti 2p$_{1/2}$ (~465.3 eV) peaks and satellite double structure at higher binding energy values. However, only the spectra of LSCTF10–45, LSCTF5–48 samples exposed in H_2 have an additional bump at low binding energy side of Ti 2p$_{3/2}$ peak. This extra signal at around 457 eV indicates the gain of electrons by Ti ions and can be identified as a signal of Ti^{3+}. The comparison of photoelectron spectra of LSCFT-45 sample shows also broadening of Ti 2p$_{3/2}$ peak and slight increase of intensity for the Ti 2p$_{1/2}$. These effects may be correlated with the change of the stoichiometry due to higher (10% instead of 5%) A-site deficiency and the oxidizing atmosphere. High stability of Ti in LSCTF5–48 (Fig. 5d) at different gas environments is in good accordance with electrochemical data.

To compare the concentration of chemical elements at the surface of the samples the overview spectra of Ti 2p, Ca 2p and Sr 3p were collected (presented in Fig. S2 in supplementary). No remarkable changes of the elemental concentrations depending on the magnitude of A-site deficiency level was detected. The samples with different (5% or 10%) A-site deficiency follow the same elemental concentration trends at their surfaces. However, the drastic change of satellite structure of Ca 2p at around 358 eV depending on its concentration level has been noticed. This shape of satellites does not show correlation with the magnitude of A-site deficiency level. However, the changes in the satellite structure refer to the variations in the stoichiometry or decomposition of perovskite to composite oxides on the surface of samples.

The other B-site component of these samples is Fe cations with approximately 20 times lower bulk concentration compared with Ti cations. The concentration level of Fe ions in all samples is closest to the detection limit of XPS signal compared to the other chemical elements of present samples. Due to this circumstance the recording of Fe 2p photoelectron signal showed quite low signal-to-background ratio. However, there was drastic discrepancy between data for the reduced and oxidized samples. For example, the oxidized LSCTF5–48 (exposed in air) has approximately 14 times higher signal-to-background ratio compared to the reduced LSCTF5–48 (exposed in H_2). In other words, all oxidized samples showed remarkably stronger Fe 2p photoelectron signal compared to the reduced samples. This phenomenon could be explained by the concentration of Fe to the Fe-rich dots (Fig. 3) and decrease of Fe concentration from other surface areas as a result of sample reduction. This process finally leads to the lower Fe concentration exposed for X-rays in the case of the reduced samples compared to the oxidized samples.

The Fe 2p photoelectron spectra have a broad multiple structure. The multiple splitting is caused by the presence of unpaired electrons of photoionized Fe cations. Due to the created core hole there can be coupling between the unpaired core electron with the unpaired outer shell electron. This can lead to creation of several final states and cause multiple peaks in photoelectron spectrum. Here we present the fitting results of Fe 2p$_{3/2}$ photoelectron spectrum of oxidized LSCTF5–48 sample (Fig. 6). The used fitting model is based on the Gupta and Sen (GS) multiple parameters, described more precisely in Ref. 40. Our results are presented in Fig. 6. This spectrum has a broad peak with a shoulder on the low binding energy side resembling Fe_3O_4 spectrum.[40] The weak bump on the high energy side can be identified as a shake-up satellite peak of the Fe^{2+} cations. The estimation of corresponding peak areas enables to calculate the Fe^{3+}/Fe^{2+} ratio. It was found to be 0.73:1. The presence of Fe_2O_3 contribution is also confirmed by visual inspection of corresponding samples. The oxidized samples were red-brown coloured and reduced samples had black-grey surfaces.

***TOF-SIMS analysis of electrode-electrolyte cross-sections.*—**SIMS measurements were performed to all electrode-electrolyte interfaces prepared during this study to investigate Sr mobility during sintering. The TOF-SIMS analysis results from cross-sections of two selected cells of LSCTF5-x after sintering for 5 h at 1250 °C are shown in Fig. S3. As can be seen in Fig. S3, Sr mobility and accumulation of Sr to the interlayer between GDC and electrolyte was not observed. Therefore, SIMS measurements approve relatively low Sr mobility during thermal treatment, which can be explained by stabilizing effect of Fe-dopant for the A-site cations.[35,41]

***Electrical properties of porous electrode.*—**In order to study the effect of A-site modification on the electrical properties of fuel electrodes, total electrical conductivities of porous LSCTF5-x layers were measured with respect to temperature variation in the range from 650 to 850 °C in air, 97% H_2 + 3% H_2O and in 1%H_2 + 3% H_2O + 96% Ar, by using the DC four-probe method. Table II shows the values of electrical conductivity of porous LSCTF5-x fuel

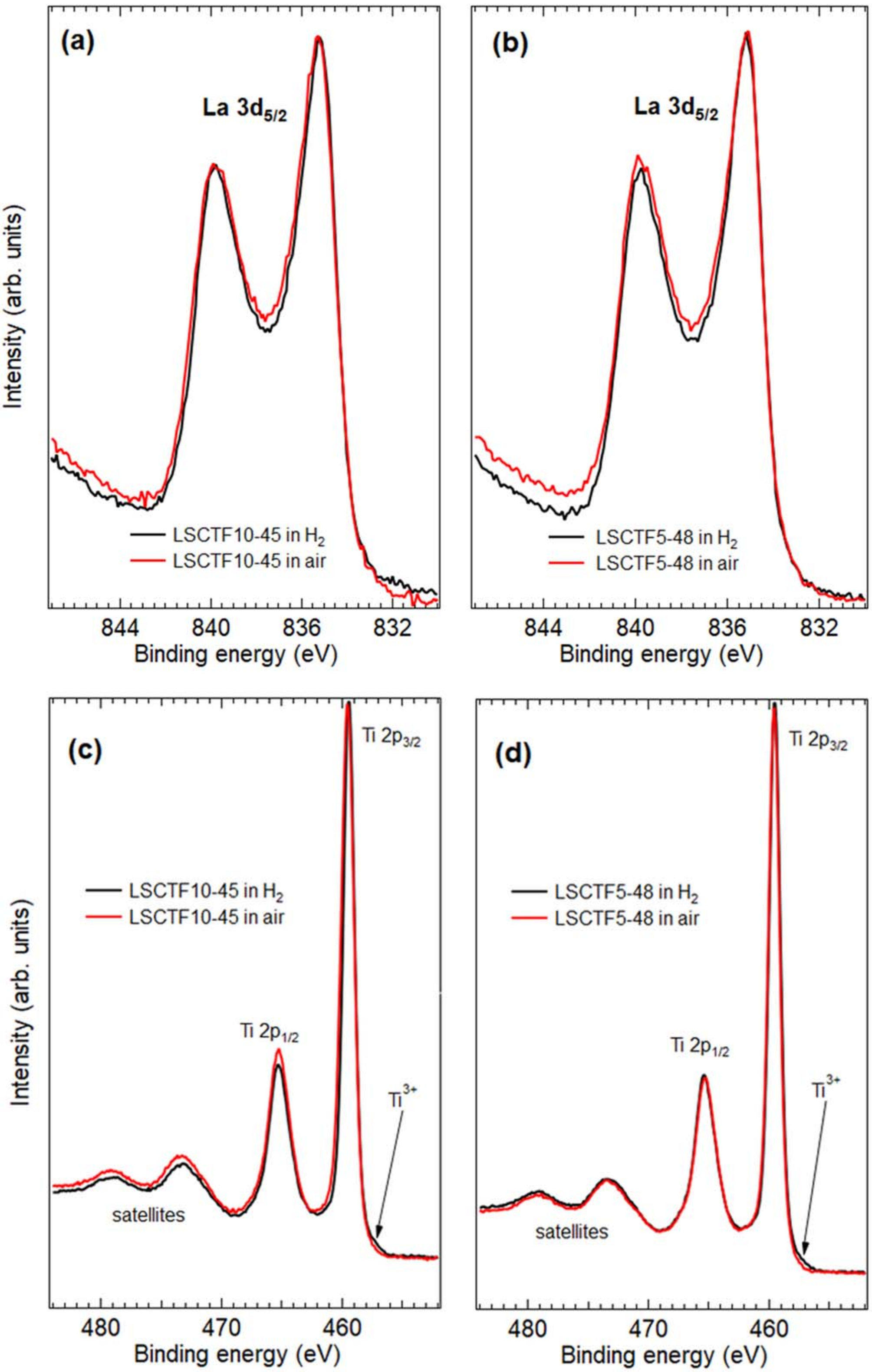

Figure 5. Comparison of La 3d electron spectra in reducing and in oxidizing atmosphere for (a) LSCTF10–45, (b) LSCTF5–48 samples, the Ti 2p photoelectron spectra of (c) LSCTF10–45 and (d) LSCTF-48 anode materials. Both samples were exposed and annealed in H_2 or in air atmosphere.

electrodes recorded after 24 h of in situ reduction in hydrogen environment at 850 °C and they are compared with electrical conductivity of porous LSCTF10-x fuel electrodes reported in our previous study.[35] All different compositions show poor conductivity in air which can be explained by insufficient oxygen vacancy concentration and high activation energy for oxide ions and oxygen vacancies in the LSCTF5-x lattice, as well as by n-type conduction mechanism of titanate, which leads to decrease of electronic conductivity at higher oxygen partial pressures. The electrical conductivities of all studied compositions in the temperature range of 650 °C–850 °C in 97% H_2 + 3% H_2O and 1% H_2 + 3% H_2O + 96% Ar gas atmospheres are presented in Figs. S4a, S4b. These

Table II. Conductivities (at 850 °C) and activation energies (650 °C–850 °C) of LSCTF5 -x samples in 97% H_2 + 3% H_2O and 1%H_2 + 3% H_2O + 96% Ar atmospheres.

Gas composition	Composition	LSCTF5–26	LSCTF5–37	LSCTF5–48	LSCTF5–58	LSCTF5–69
97% H_2 + 3% H_2O	Conductivity (S cm^{-1})	1.9	3.1	3.5	3.45	2.79
97% H_2 + 3% H_2O	Activation energy (eV)	0.34	0.32	0.36	0.41	0.37
1%H_2 + 3% H_2O + 96% Ar	Conductivity (S cm^{-1})	0.41	0.83	1	0.77	0.77
1%H_2 + 3% H_2O + 96% Ar	Activation energy (eV)	0.49	0.52	0.57	0.63	0.6

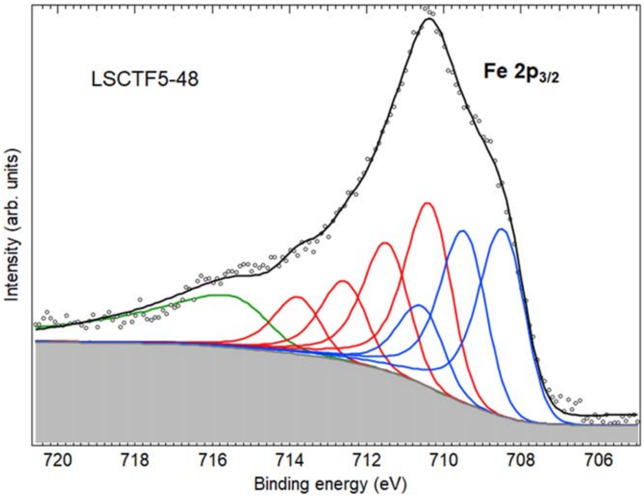

Figure 6. The Fe $2p_{3/2}$ photoelectron spectrum of oxidized LSCTF5–48 sample. The Fe^{3+}(red lines) and Fe^{2+} (blue lines) multiple peaks are presented together with Shirley background (grey), Fe^{2+} satellite peak (green line), fitting result (black line) and experimental data (o - markers).

graphs confirm the increase of electrical conductivity with increasing temperature in both atmospheres and also demonstrate the semiconductor-like behaviour of all materials studied.

According to Table II, similarly to LSCTF10-x dataset,[35] the electrical conductivity depends on the magnitude of A-site deficiency and also Ca dopant level which is shown in Figs. S4c, S4d. Comparing to the best conductivities measured during this study (LSCTF5–48), the LSCTF10–45 which has 10% A-site deficiency showed higher conductivity values, 5.5 S cm^{-1} and 1.8 S cm^{-1} in the 97% H_2 + 3% H_2O and 1%H_2 + 3% H_2O + 96% Ar atmosphere at 850 °C, respectively.[35] It confirms that the LSCTF with higher deficiency has also higher electrical conductivity. In fact, increase of the magnitude of A-site deficiency contributes to charge compensation phenomena through the additional oxidation of B-site elements which leads to decrease of Ti-O length and improve polaron hopping. The improved sintering density at higher magnitude of A-site deficiency could be additional contribution to conductivity.[42] Increase of the magnitude of A-site deficiency also leads to the increase of the concentration of oxide ion vacancies, therefore increase of oxide ion conductivity, which might lead to increase of unit cell volume and negative influence on the electronic conductivity. In addition, in both A-site deficiencies for the lowest Ca contents, conductivities were very low, probably reflecting the low crystallinity and slightly worse conductivity of bulk phase; Samples with higher calcium content showed a slightly higher crystallinity which indicates that calcium doping did improve the densification and crystallinity of these materials and the LSCTF-48 sample gave both the highest crystallinity and conductivity in the series. In fact, the crystallinity of each of the tested samples are in accordance with the conductivity values obtained in this study (Fig. 2). However, as calcium content increased further, the conductivity of the samples with higher calcium content decreased as shown in Figs. S4c, S4d. These results indicate that Ca dopant level influence the electrical conductivity of the material.

The experimental results confirm that the conductivity is also significantly influenced by oxygen partial pressure. It appears, that 70 to 80% decrease of conductivity results from the change of gas environment from 97% H_2 + 3% H_2O gas mixture with oxygen partial pressure, pO_2, from 4.29 × 10^{-26} to 4.16 × 10^{-21} atm to 1% H_2 + 3% H_2O + 96% Ar gas mixture with the pO_2 from 4.04 × 10^{-22} to 4.04 × 10^{-17} atm in the temperature range from 650 to 850 °C.[35] Increase of conductivity as a result of decrease of oxygen partial pressure has been explained by release of oxygen from the perovskite lattice which leads to the creation of oxide ion vacancies and accompanying reduction of Ti^{4+} to Ti^{3+} leading to the semiconducting behaviour and increase of electronic conductivity in material.

The Arrhenius plots for all LSCTF5-x samples in the temperature range from 650 to 850 °C were calculated and the activation energies were stablished (Figs. S4e, S4f). Sufficient linearity of Arrhenius plots was obtained for all samples, which indicates that the conduction mechanism does not change significantly in studied temperature range in the case of particular compositions. The variation of activation energy of conduction process as a function of material composition (magnitude of A-site deficiency and Ca concentration) or gas atmosphere indicates the change of limiting conduction mechanism during aforementioned manipulations. Decrease of E_a from 0.54 eV to 0.36 eV if A-site deficiency is changed from 10 to 5 percent for composition with x = 45, indicates that both LSCTF10-x and LSCTF5-x compositions are mixed conductors but the nature of rate limiting conduction process shifts to more electronic conductivity,[35] i.e. increase of the magnitude of A-site deficiency leads to higher number of oxide ion vacancies and higher oxide ion conductivity.

Variation of Ea from 0.32 eV (LSCTF5–37) to 0.41 eV (LSCTF5–58) in LSCTF-x with 5% A-site deficiency as a function of Ca dopant shows that the nature of rate limiting conduction process is more electronic conductivity in LSCTF5–37 compared to LSCTF5–58. The differences between activation energies in this set of materials are small and can be related to differences in microstructure.[43] Moreover, the decrease of activation energy with decrease of pO_2 indicates higher fraction of electronic conductivity in the total conductivity.

Electrochemical analysis of symmetric cells.—To evaluate the effect of A-site modification on the electrochemical properties of LSCTF5-x electrodes and to study the initial mid-term stability of electrodes, the impedance analysis of the symmetrical cells with LSCTF5-x electrodes have been performed under different oxygen partial pressures and temperatures. In fact, two different gas mixtures, 98.3% H_2 + 1.7% H_2O (pO_2 = 1.3 × 10^{-21} atm at 850 °C and pO_2 = 1.34 × 10^{-26} at 650 °C) and 1% H_2 + 1.7% H_2O + 97.3% Ar (pO_2 = 1.26 × 10^{-17} atm at 850 °C and pO_2 = 1.3 × 10^{-22} atm at 650 °C) were used in the measurements of all samples.

The comparison of polarization resistance (R_p) values of both LSCTF5-x and LSCTF10-x[35] electrodes at constant pO_2 and temperature are shown in Fig. 7. All R_p values reported in this study are measured after 100 h reduction/stabilization at 800 °C (Fig. 7). From electrochemical studies of symmetric cells it seems that there is steady increase of R_p values for all studied LSCTF5-x electrodes exposed to the 98.3% H_2 + 1.7% H_2O gas mixture at 800 °C in time (Fig. S5). All R_p values reported are measured after 100 h reduction/stabilization at 800 °C (Fig. 7, Table III). From

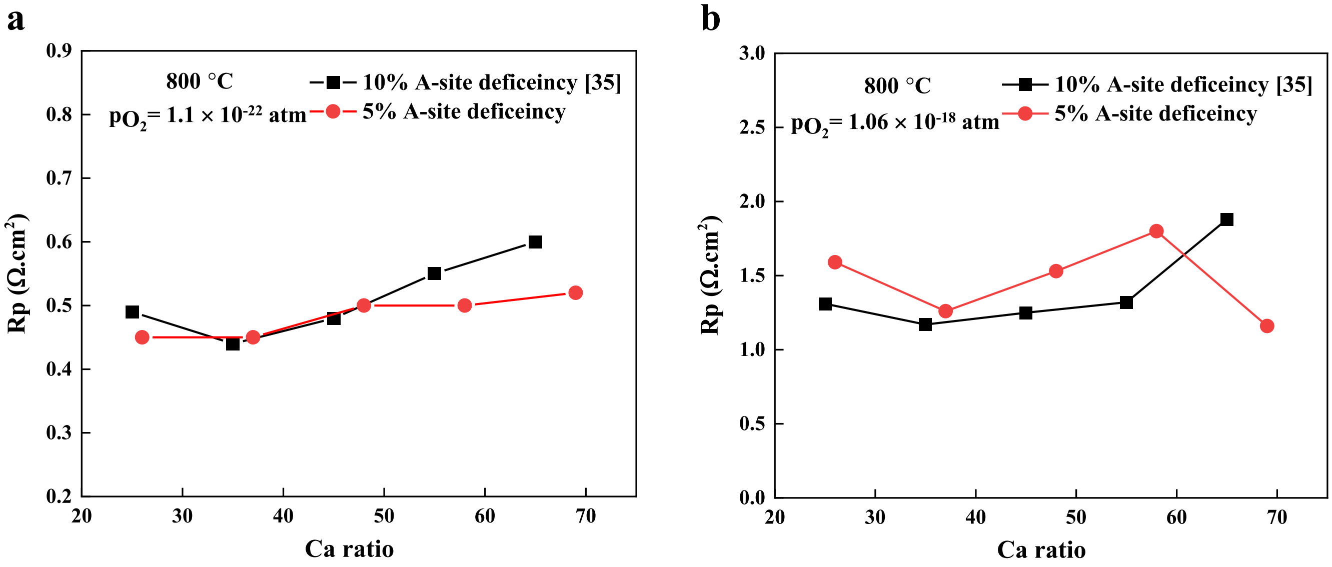

Figure 7. Polarization resistance (R_p) of LSCTF10-x and LSCTF5-x samples in 98.3% H_2 + 1.7% H_2O atmosphere as a function of Ca doping after 100 h stabilization at 800 °C (a) and in 1%H_2 + 1.7% H_2O + 97.3% Ar atmospheres after 24 h stabilization at 800 °C (b).[35]

electrochemical studies of symmetric cells seems that there is steady increase in R_p values of all studied LSCTF5-x electrodes exposed to the 98.3% H_2 + 1.7% H_2O gas mixture at 800 °C in time (Fig. S5) and it could be noticed that LSCTF5–37 was the most stable material and LSCTF5–69 was the most unstable composition during the 100 h application. As it can be seen in Fig. 7, LSCTF10–35 and LSCTF5–37 are most active materials at two different A-site deficiencies and at two different oxygen partial pressures while LSCTF10–65 is electrode with highest R_p values. Low R_p for LSCTF5–69 at high oxygen partial pressures could be explained as a result of instabilities of the MIEC lattice, which leads to high activity at certain degradation stage. In general, these results (Fig. 7) indicate that Ca dopant level influence not only the electrical conductivity of the material, but also has some effect on the electrocatalytic properties of the surface.

The high frequency (HF) and low frequency (LF) polarization resistance, R_{HF} and R_{LF}, values for LSCTF5-x samples were obtained by applying complex nonlinear least square fitting (CNLS) of $R_s(R_{HF}CPE_{HF})(R_{LF}CPE_{LF})$ equivalent circuit to the experimental Nyquist plots (Table III). Dependence of R_{LF} and R_{HhF} on electrode composition, oxygen partial pressure and temperature were studied to understand the nature of the LF and HF processes. The activation energies were calculated from the Arrhenius plots of the LF and HF resistance values in temperature range from 650 to 800 °C and are shown in Table III.

Based on Table III, E_{actHF} values for LSCT5-x samples in the frequency range from 10^3 to 10^2 Hz are close to 1 eV, which means, that HF process could be associated to the mobility of ions in the the grain boundaries of MIEC|electrolyte or MIEC|MIEC grains, diffusion of charged species to the TPB of MIEC and electrolyte and also mass transfer of ions in the MIEC close to the current collector.[18,44–46] LF process in the frequency range from 100 to 0.01 Hz and with activation energies from 0.4 to 0.9 eV could be attributed to the gas-solid adsorption and surface-exchange process, including also solid-state diffusion gas phase diffusion and conversion.[35,45–47]

From the analysis of experimental results appears that the activation energies of HF and LF processes are dependent on the chemical composition of A-site, the magnitude of A-site deficiency and gas composition. The activation energies of the HF process in 98.3% H_2 + 1.7% H_2O atmosphere are in the range from 1.06 eV (for

Table III. Polarization resistance (R_p), high frequency resistance (R_{HF}) and low frequency resistance (R_{LF}) of LSCTF5-x samples in 98.3% H_2 + 1.7% H_2O atmosphere (a) after 100 h stabilization at 800 °C and in 1% H_2 + 1.7% H_2O + 97.3% Ar atmosphere (b) after 24 h stabilization at 800 °C and activation energy values in temperature range from 650 °C to 800 °C.

Composition	LSCTF5–26	LSCTF5–37	LSCTF5–48	LSCTF5–58	LSCTF5–69
			(a)		
Rp (Ω.cm^2)	0.45	0.45	0.5	0.5	0.52
RHF (Ω.cm^2)	0.039	0.037	0.042	0.032	0.043
RLF (Ω.cm^2)	0.41	0.42	0.46	0.47	0.48
Eact (eV)	0.876	0.73	0.92	0.89	0.81
EactHF (eV)	1.14	1.08	1.09	1.27	1.06
EactLF (eV)	0.83	0.68	0.89	0.84	0.78
			(b)		
Rp (Ω.cm^2)	1.59	1.26	1.53	1.8	1.16
RHF (Ω.cm^2)	0.029	0.035	0.035	0.022	0.029
RLF (Ω.cm^2)	1.55	1.23	1.50	1.78	1.137
Eact (eV)	0.51	0.42	0.55	0.54	0.52
EactHF (eV)	1.22	1.08	1.17	1.4	1.23
EactLF (eV)	0.48	0.38	0.5	0.52	0.48

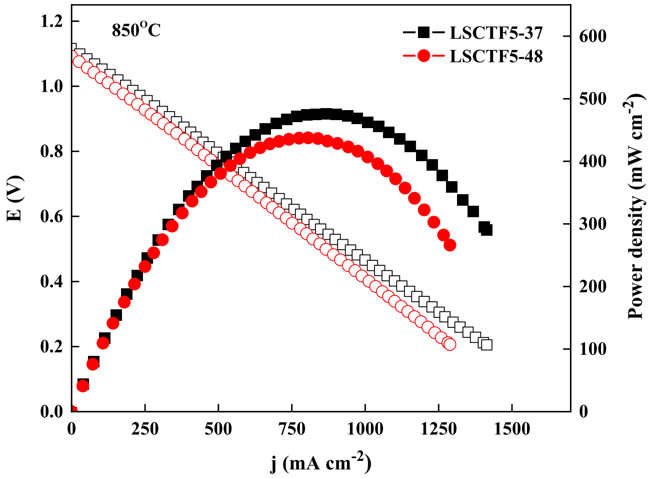

Figure 8. j vs V (scan rate 5 mV s^{-1}) and j vs P curves of the fuel cells based on LSCTF5–37 and LSCTF5–48.

LSCT5–69) to 1.27 eV (for LSCTF5–58), whereas the range of activation energy for the LF process is between 0.68 eV (for LSCTF5–37) and 0.89 eV (for LSCTF5–48). General trend is that changing of A site deficiency from 5 to 10% leads to the decrease of activation energy. However, all samples do not follow the same trend and in the case of LSCTF5–37 (at high pO_2) and LSCTF5–69 (at both pO_2-s), the activation energy of high frequency process increasing by increasing the magnitude of A-site deficiency.[35] Very high E_{actHF} values of LSCTF10–65 could be explained by poor stability of this material. LSCTF5–37 and LSCTF10–45 compositions indicate the lowest activation energy values between both 5 and 10% A-site deficiency.[35]

By changing the gas atmosphere from 98.3% H_2 + 1.7% H_2O to 1% H_2 + 1.7% H_2O + 97.3% Ar, material properties change which is also exposed in the Nyquist response of symmetrical cell (Fig. S6a). All symmetric cells were exposed to 1% H_2 + 1.7% H_2O + 97.3% Ar atmosphere ($pO_2 = 1.1 \times 10^{-18}$ atm) for 24 h at 800 °C in order to evaluate the impact of oxygen partial pressure on the initial stability of studied electrodes and the change of R_p over time is shown in Fig. S6b. The electrochemical performance of all compositions from first hour of stabilization, illustrated almost a constant behaviour which confirm the positive effect of higher oxygen partial pressure on the stability of the electrochemical performance of the studied materials and also indicates that most of changes has been already occurred during 100 h measurements in gas environment with lower pO_2. The numerical values of R_p, R_{HF}, and R_{LF} at the $pO_2 = 1.1 \times 10^{-18}$ atm are presented in Table IIIb. Impedance data of LSCTF5-x show similar behaviour as LSCTF10-x,[35] i.e. the HF resistance, R_{HF}, and the HF activation energy, E_{actHF}, changed slightly with increase of pO_2. Relative stability of HF process parameters shows that this process is very likely connected with the oxide ion conductivity in the MIEC electrode. However, the LF resistance, R_{LF}, values show significant increase with the increase of pO_2 which could be related to the decrease of the surface concentration of adsorbing H_2 atoms. The variation of activation energy (E_{actLF}) confirms the change of the geometry of active adsorption sites because of the change of pO_2.

LSCTF5–37 and LSCTF5–48 have been assumed as the most active materials with highest electrochemical properties and electrical conductivity, respectively, at both gas compositions and were selected for the tests in fuel-cell mode.

The activation energies of high-frequency process characterised by series resistance, R_s, are also affected by the change of the magnitude of A-site deficiency (Fig. S7) and E_{actRs} decreases with the increase of the magnitude of A-site deficiency. The A-site deficient composition should promote the exsolution of B-site dopant (Fe) to increase the catalytic activity. As the active surface area of MIEC depends on the electronic conductivity of MIEC material, increased electronic conductivity can be also the reason for the decrease of activation energy.

Electrochemical characterization of fuel electrodes in fuel cell mode.—The electrochemical performance of porous LSCTF5–37 and LSCTF5–48 electrodes were characterized in solid oxide fuel cell mode by using following MEA configurations: LSCTF5–37/(GDC)/GDC/ScCeSZ/GDC/LSCT and LSCTF5–48/(GDC)/GDC/ScCeSZ/GDC/LSCT. Both button cells were measured using 2-electrode configuration in 98.3% H_2 + 1.7% H_2O atmosphere at 850 °C (Fig. 8). As can be seen in Fig. 8, highest peak power density of 476 mW cm^{-2} was measured in the case of the fuel cell with the LSCTF5–37 anode and it was 8% higher than the peak power density of cell with LSCTF5–48 anode (437 mW cm^{-2}).

The electrochemical impedance spectroscopy results of LSCTF5–37 and LSCTF5–48 in solid oxide fuel cell are compared with LSCTF10–35 and LSCTF10–45 measured at similar

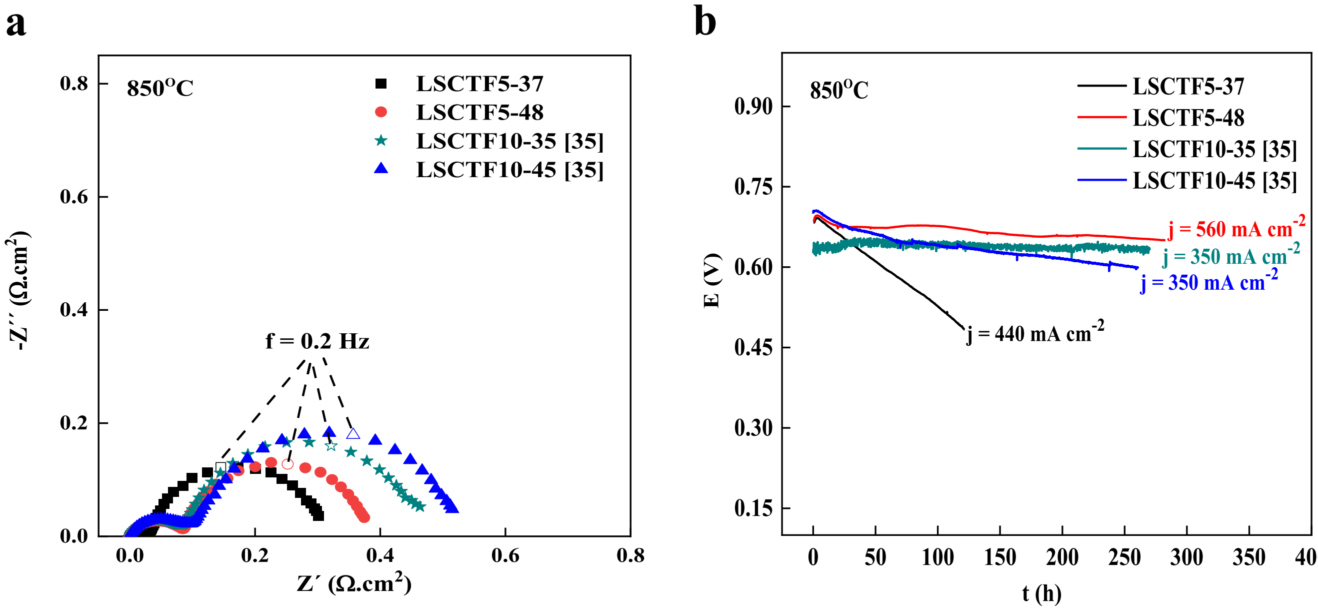

Figure 9. (a) Nyquist plots of the fuel cells based on LSCTF5–37, LSCTF5–48, LSCTF10–35 and LSCTF10–45 at 850 °C, (b) dependence of the cell voltage on the time of fuel cells based on LSCTF10–35, LSCTF10–45, LSCTF5–37 and LSCTF5–48 anodes measured in the 98.3% H_2+1.7% H_2O atmosphere at 850 °C.[35]

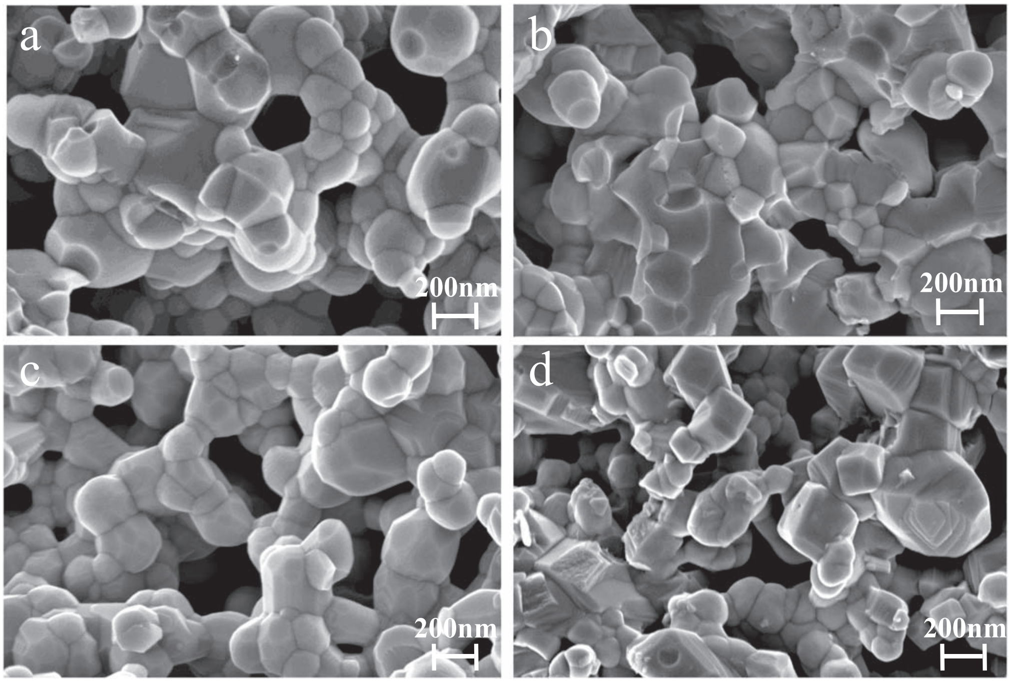

Figure 10. SEM images of the cross section of the porous anode layers of $La_{0.21}Sr_{0.37}Ca_{0.37}Ti_{0.95}Fe_{0.05}O_{3-\delta}$ (LSCTF5–37) (a) and $La_{0.21}Sr_{0.26}Ca_{0.48}Ti_{0.95}Fe_{0.05}O_{3-\delta}$ (LSCTF5–48) (b) before the fuel-cell durability test and for LSCTF5–37 (c) and LSCTF5–48 (d) after the 160 h and 280 h fuel-cell operation, respectively.

conditions[35] to evaluate the influence of A- site deficiency as shown in (Fig. 9a). The polarization resistance of LSCTF5–37, LSCTF5–48, LSCTF10–35 and LSCTF10–45 cells are calculated and found to be 0.311, 0.38, 0.46 and 0.52 $\Omega.cm^2$ at 850 °C, respectively.[35] Smaller R_p values for 5% deficient materials are in accordance with XRD results which show more stable lattice structure (and surface with higher number of active centres) in the case of lower magnitude of A-site deficiency.

The stability of LSCTF5–37 and LSCTF5–48 based fuel electrodes was further evaluated and compared with the stability of LSCTF10–35 and LSCTF10–45 based anodes at operating conditions of the SOFC single cells at a constant current density at 850 °C for more than 250 h and it is given in Fig. 9b.[35] It appears that the cell voltage of LSCTF5–48 anode based fuel cell at 560 mA cm^{-2} over the 270 h at 850 °C durability test, decreased 0.03 V (0.8%/100 h). However, the voltage dropped sharply and approximately linearly with 15.7%/100 h rate in the case of fuel cell based on LSCTF5–37 under constant current density 440 mA cm^{-2} at 850 °C and shown in Fig. 9b. As can be observed from Fig. 9b, the cell voltage for fuel cell based on LSCTF10–35 and LSCTF10–45 decreased with the rate 0.5%/100 h and 2.7%/100 h, respectively.[35] It is worth to conclude that LSCTF5–48 anode with 5% A-site deficiency shows higher cell performance compared to LSCTF with 10% deficiency and also considerably good stability (almost similar with LSCTF10–35) during long-term operation, makes it most stable electrode of the measured electrode compositions in the fuel cell mode after 270 h test.

Post-test analysis on the microstructure of the anodes was carried out for the cells in order to reveal the stability of anode structure and it is shown in Fig. 10. SEM images of the cross section of the porous anode layers measured before and after long term fuel cell operation confirm similarity of the LSCTF5–37 and LSCTF5–48 anodes microstructure before and after 160 h and 280 h fuel cell operation, respectively, without any noticeable structural changes at the surface of the electrode.

Conclusions

In this study the influence of A-site modification on the electric properties as well as electrochemical performance, and to the short-term degradation and to the chemical composition of the surface of $La_{0.21}Sr_{0.74-x}Ca_xTi_{0.95}Fe_{0.05}O_{3-\delta}$ (x = 0.26 – 0.69) (LSCTF5-x) fuel electrode, have been investigated by applying different gas atmospheres and feeding conditions. According XRD analysis data, the unit cell volume of $La_{0.21}Sr_{0.74-x}Ca_xTi_{0.95}Fe_{0.05}O_{3-\delta}$ decreases continuously with the increase of Ca concentration in the A-site. The TOF-SIMS analysis confirms that thermal treatment of electrodes does not cause Sr mobility through GDC barrier layer in case of materials studied. Electrical properties of porous fuel electrodes, established by using four-probe conductivity measurements, illustrate that conductivity of the LSCTF5-x depends on the Ca concentration, and the maximum total electrical conductivity of 3.5 S cm^{-1} in 97% H_2 + 3% H_2O atmosphere at 850 °Cwas obtained for LSCTF5–48. The electrochemical performance of the synthesized materials was measured using a two electrode setup. EIS measurement data show that the catalytically most active compositions was LSCTF5–37, which had the lowest polarization resistance of 0.44 Ω cm^2 in the 98.3% H_2–1.7% H_2O (P_{O2} = 1.1 × 10^{-22}) atmosphere at 800 °C after 100 h in reducing atmosphere with lowest degradation rate. Under the realistic fuel cell working conditions, which were applied for LSCTF5–37/(GDC)/GDC/ScCeSZ/GDC/LSCT and LSCTF5–48/(GDC)/GDC/ScCeSZ/GDC/LSCT button cells, the optimal composition would be LSCTF5–48 with the peak power densities of 437 mW cm^{-2} and R_p value of 0.38 $\Omega.cm^2$ at 850 °C, offering the best stability and showing the smallest degradation during tests conducted.

Acknowledgments

This work was supported by the Estonian Research Council grants Mobilitas+ MOBJD538 and PRG551 and by EU through the European Regional Development Fund (TK141 “Advanced materials and high-technology devices for energy recuperation systems”). The TOF-SIMS research was conducted using the NAMUR+ core facility funded by the Estonian Research Council (TT 13) and was supported by ERDF project Centre of Technologies and Investigations of Nanomaterials (NAMUR+, project number 2014–2020.4.01.16–0123).

ORCID

E. Lust https://orcid.org/0000-0002-7942-1558
G. Nurk https://orcid.org/0000-0002-0673-0042

References

1. J. W. Fergus, *Solid State Ionics*, **177**, 1529 (2006).
2. S. Paydar, M. H. Shariat, and S. Javadpour, *J. Alloys Compd.*, **682**, 238 (2016).
3. S. Paydar, I. Gholaminezad, H. Shirani-Faradonbeh, S. Imanlou, N. Akbar, and M. H. Paydar, *J. Mater. Sci., Mater. Electron.*, **32**, 11129 (2021).
4. M. Maide, K. Lillmaa, L. K. Salvan, P. Möller, M. Uibu, E. Lust, and G. Nurk, *Fuel cells*, **18**, 789 (2018).
5. T. H. Shin, S. Ida, and T. Ishihara, *J. Am. Chem. Soc.*, **133**, 19399 (2011).
6. T. H. Shin, P. Vanalabhpatana, and T. Ishihara, *J. Electrochem. Soc.*, **157**, B1896 (2010).
7. M. Gong, X. Liu, J. Trembly, and C. Johnson, *J. Power Sources*, **168**, 289 (2007).
8. G. Nurk, K. Kooser, S. Urpelainen, T. Käämbre, U. Joost, M. Kodu, I. Kivi, R. Kanarbik, E. Kukk, and E. Lus, *J. Power Sources*, **378**, 589 (2018).
9. J. Sunarso, S. S. Hashim, N. Zhu, and W. Zhou, *Prog. Energy Combust. Sci.*, **61**, 57 (2017).
10. B. Li, S. He, J. Li, X. Yue, J. T. S. Irvine, D. Xie, J. Ni, and C. Ni, *ACS Catal.*, **10**, 14398 (2020).
11. A. Atkinson, S. A. Barnett, R. J. Gorte, and J. T. S. Irvine, *Nat. Mater.*, **3**, 17 (2004).
12. T. Ishihara, Perovskite oxide for solid oxide fuel cells (fuel cells and hydrogen energy) (2009).
13. P. K. Tiwari, X. Yue, J. T. S. Irvine, and S. Basu, *J. Electrochem. Soc.*, **164**, F1030 (2017).
14. M. C. Verbraeken, B. Iwanschitz, A. Mai, and J. T. S. Irvine, *J. Electrochem. Soc.*, **159**, F757 (2012).
15. X. Li, H. Zhao, N. Xu, X. Zhou, C. Zhang, and N. Chen, *Int. J. Hydrog. Energy.*, **34**, 6407 (2009).
16. X. Zhou, N. Yan, K. T. Chuang, and J. Luo, *RSC Adv.*, **4**, 118 (2014).
17. A. Gondolini, E. Mercadelli, G. Constantin, L. Dessemond, V. Yurkiv, R. Costa, and A. Sanson, *J. Eur. Ceram. Soc.*, **38**, 153 (2018).
18. H. Tanaka, M. Uenishi, M. Taniguchi, I. Tan, K. Narita, M. Kimura, K. Kaneko, Y. Nishihata, and J. Mizuki, *Catal. Today*, **117**, 321 (2006).
19. B. D. Madsen, W. Kobsiriphat, Y. Wang, L. D. Marks, and S. Barnett, *ECS Trans.*, **7**, 1339 (2007).
20. D. Neagu, G. Tsekouras, D. N. Miller, H. Ménard, and J. T. S. Irvine, *Nat. Chem.*, **5**, 916 (2013).
21. M. Chanthanumataporn, J. Hui, X. Yue, K. Kakinuma, J. T. S. Irvine, and K. Hanamura, *Electrochim. Acta*, **306**, 159 (2019).
22. M. Maide, P. Paiste, P. Möller, E. Lust, and G. Nurk, *J. Electrochem. Soc.*, **166**, F1148 (2019).
23. A. D. Aljaberi and J. T. S. Irvine, *J. Mater. Chem. A*, **1**, 5868 (2013).
24. J. Feng, J. Qiao, W. Wang, Z. Wang, W. Sun, and K. Sun, *Electrochim. Acta*, **215**, 592 (2016).
25. O. A. Marina, N. L. Canfield, and J. W. Stevenson, *Solid State Ionics*, **149**, 21 (2002).
26. X. Li, H. Zhao, F. Gao, N. Chen, and N. Xu, *Commun.*, **10**, 1567 (2008).
27. T. McColm and J. Irvine, *Ionics*, **7**, 116 (2001).
28. Y. Zhu, Z. G. Chen, W. Zhou, S. Jiang, J. Zou, and Z. Shao, *ChemSusChem*, **6**, 2249 (2013).
29. G. Yang, J. Feng, W. Sun, N. Dai, M. Hou, X. Hao, J. Qiao, K. Sun, and J. Power, *Sources*, **268**, 771 (2014).
30. A. Mineshige, J. Izutsu, M. Nakamura, K. Nigaki, J. Abe, M. Kobune, S. Fujii, and T. Yazawa, *Solid State Ionics*, **176**, 1145 (2005).
31. W. Lee and B. Yildiz, *ECS Trans.*, **57**, 2115 (2013).
32. W. Zhou, R. Ran, Z. Shao, W. Jin, and N. Xu, *J. Power Sources*, **182**, 24 (2008).
33. N. Muzaffar, N. Arshad, N. Firdous, D. B. Drasbæk, B. R. Sudireddy, and P. Holtappels, *Mater. Chem. Phys.*, **270**, 124875 (2021).
34. A. Yaqub, N. K. Janjua, C. Savaniu, and J. T. S. Irvine, *Int. J. Hydrogen Energy*, **40**, 760 (2015).
35. S. Paydar, K. Kooser, P. Möller, O. Volobujeva, S. Granroth, E. Lust, and G. Nurk, *ACS Appl. Energy Mater.*, **5**, 10119 (2022).
36. I. Kivi, J. Aruväli, K. Kirsimäe, A. Heinsaar, G. Nurk, and E. Lust, *J. Electrochem. Soc.*, **162**, F354 (2015).
37. E. Kukk et al., *Phys. Rev. Lett.*, **95**, 133001 (2005).
38. E. Kukk, G. Snell, J. D. Bozek, W. T. Cheng, and N. Berrah, *Phys. Rev. A - At. Mol. Opt. Phys.*, **63**, 062702 (2001).
39. R. Price, M. Cassidy, J. G. Grolig, G. Longo, U. Weissen, A. Mai, and J. T. S. Irvine, *Adv. Energy Mater.*, **11**, 2003951 (2021).
40. A. P. Grosvenor, B. A. Kobe, M. C. Biesinger, and N. S. McIntyre, *Surf. Interface Anal.*, **36**, 1564 (2004).
41. B. Koo, K. Kim, J. K. Kim, H. Kwon, J. W. Han, and W. C. Jung, *Joule*, **2**, 1476 (2018).
42. L. Ge, W. Zhou, R. Ran, S. Liu, Z. Shao, W. Jin, and N. Xu, *J. Memb. Sci.*, **306**, 318 (2007).
43. A. Yaqub, C. Savaniu, N. K. Janjua, and J. T. S. Irvine, *J. Mater. Chem. A*, **1**, 14189 (2013).
44. R. Küngas, A. S. Yu, J. Levine, J. M. Vohs, and R. J. Gorte, *J. Electrochem. Soc.*, **160**, F205 (2013).
45. R. Barfod, M. Mogensen, T. Klemensø, A. Hagen, Y. L. Liu, and P. Vang Hendriksen, *Proc. - Electrochem. Soc., PV*, **2005–07**, 524 (2005).
46. L. Almar, J. Szász, A. Weber, and E. Ivers-Tiffée, *J. Electrochem. Soc.*, **164**, F289 (2017).
47. A. Torabi and T. H. Etsell, *J. Power Sources*, **225**, 51 (2013).